Multiple ionization and coupling effects in *L*-subshell ionization of heavy atoms by oxygen ions

M. Pajek,* D. Banaś, J. Semaniak, J. Braziewicz, U. Majewska, and S. Chojnacki†
Institute of Physics, Świętokrzyska Academy, 25-406 Kielce, Poland

T. Czyżewski, I. Fijał, and M. Jaskóła
The Andrzej Soltan Institute for Nuclear Studies, 05-400 Otwock-Świerk, Poland

A. Glombik and W. Kretschmer
Physikalisches Institüt, Universität Erlangen-Nürnberg, D-91058 Erlangen, Germany

D. Trautmann
Institüt für Physik, Universität Basel, CH-4056 Basel, Switzerland

G. Lapicki
Department of Physics, East Carolina University, Greenville, North Carolina 27858, USA

T. Mukoyama
Kansai Gaidai University, Hirakata, Osaka 573-1001, Japan
(Received 6 December 2002; published 13 August 2003)

The multiple-ionization and coupling effects in *L*-shell ionization of atoms by heavy-ion impact have been studied by measuring the *L* x-ray production cross sections in solid targets of Au, Bi, Th, and U bombarded by oxygen ions in the energy range 6.4–70 MeV. The measured *L* x-ray spectra were analyzed using the recently proposed method accounting for the multiple-ionization effects, such as x-ray line shifting and broadening, which enables one to obtain the ionization probabilities for outer shells. The *L*-subshell ionization cross sections have been obtained from measured x-ray production cross sections for resolved $L\alpha_{1,2}$, $L\gamma_1$, and $L\gamma_{2,3}$ transitions using the *L*-shell fluorescence and Coster-Kronig yields being substantially modified by the multiple ionization in the *M* and *N* shells. In particular, the effect of closing of strong L_1-$L_3M_{4,5}$ Coster-Kronig transitions in multiple-ionized atoms was evidenced and discussed. The experimental ionization cross sections for the L_1, L_2, and L_3 subshells have been compared with the predictions of the semiclassical approximation (SCA) and the ECPSSR theory that includes the corrections for the binding-polarization effect within the perturbed stationary states approximation, the projectile energy loss, and Coulomb deflection effects as well as the relativistic description of inner-shell electrons. These approaches were further modified to include the *L*-subshell couplings within the ''coupled-subshell model'' (CSM). Both approaches, when modified for the coupling effects, are in better agreement with the data. Particularly, the predictions of the SCA-CSM calculations reproduce the experimental *L*-subshell ionization cross section reasonably well. Remaining discrepancies are discussed qualitatively, in terms of further modifications of the *L*-shell decay rates caused by a change of electronic wave functions in multiple-ionized atoms.

DOI: 10.1103/PhysRevA.68.022705 PACS number(s): 34.50.Fa, 31.70.−f

I. INTRODUCTION

Inner-shell ionization by charged particles [1,2] has been extensively investigated in last three decades, mainly because of its importance for the particle induced x-ray emission (PIXE) in analytical studies. On the other hand, an accurate knowledge of the cross sections for ionization induced by light and heavy ions over a wide energy and element ranges offers an experimental basis for developing and testing theoretical descriptions of both ionization [2–4] and inner-shell deexcitation [5,6] processes. Initially, most experiments were performed for light-ion impact for *K* and *L* shells [7–13]. Following increased availability of heavy-ion beams, inner-shell ionization measurements have been extended to heavier ions and *L* and *M* shells [14–16].

Simultaneously with experimental studies, the main theoretical effort has been focused on the description of asymmetric collisions ($Z_1 \ll Z_2$), where Z_1 and Z_2 are the projectile and target atomic numbers, respectively. In such collisions, the inner-shell vacancies are produced predominantly by the direct Coulomb ionization process, which can be treated perturbatively using the first-order perturbation approaches, namely, the plane-wave Born approximation PWBA [3] and the semiclassical approximation (SCA) [4]. Besides the quantum-mechanical treatment, the classical nonperturbative approach, known as the binary-encounter approximation (BEA) [17], was developed for describing direct ionization. This model treats the ionization process in a more simplified way and, for this reason, it will not be discussed here. The standard PWBA [18–20] and SCA [21–23] approaches for direct ionization were further developed to include the hyperbolic trajectory of the projectile [24–26],-

*Electronic address: pajek@pu.kielce.pl
†Also at Heavy Ion Laboratory, Warsaw University, 02-097 Warsaw, Poland.

the relativistic wave functions [25,27–30], and the corrections for the ''binding-polarization effect'' [31–33]. The most advanced approach based on the PWBA, which goes beyond the first-order treatment to include the corrections for the binding-polarization effects within the perturbed stationary states (PSS) approximation, the projectile energy loss (E), and Coulomb deflection (C) effects as well as the relativistic (R) description of inner-shell electrons, is known as the ECPSSR theory [34]. On the other hand, the state-of-the-art SCA calculations, which are presently available (see Refs. [35–38]), use the hyperbolic projectile trajectory and relativistic electronic wave functions in an exact way, but the binding effect can be treated within this approach in the extreme cases of separated atoms (SA) or united atoms (UA) limits.

The best description of the ionization process is found for the K and L shells for light ions in a broad range of projectile energies and target atomic numbers. Heavier projectiles, however, perturb initial electronic states more strongly and consequently, the ECPSSR and SCA theories cannot describe these data as well as for lighter ions, particularly for L-subshell ionization by low-velocity heavy ions. Serious discrepancies between the data and the theoretical predictions were reported for heavier ions such as C and N [39,40]. However, the number of experimental studies concerning L subshell ionization by ions heavier than helium is rather limited. For instance, for oxygen ions, which are discussed in this work, only a handful of experiments have been performed [14,15,41–43].

The main reason for the discrepancies observed between the data and the theoretical predictions for L subshell ionization could be the fact that the theoretical approaches mentioned above treat the ionization of L subshells independent of each other, neglecting the intrashell coupling effects. Since the electronic wave functions for the L subshells are very close to each other, both in energy and space, the dynamical couplings between the states can strongly modify the initial L shell vacancy distribution. For this reason, the strong discrepancies between the experimental results and the theoretical predictions, being as much as the order of magnitude, for L_2-subshell ionization by heavy ions of low velocity were observed [44,45].

The mechanism of vacancy sharing was first studied by Sarkadi and Mukoyama in a simple two-step model [44], which treated the creation and rearrangement of vacancies as two independent processes. Later, more refined models were developed by the same authors on the basis of the second-order Born approximation [46,47] and the simplified coupled-states model [48–51]. Full coupled-channel calculations, including the continuum, have been reported by Martir *et al.* [52], using a target-centered expansion and pseudostates for the continuum, and by Mehler *et al.* [53], using wave packets. The calculations by Mehler *et al.* [54] showed that for very asymmetric collisions, the L-subshell vacancy production is not very sensitive to the couplings in the continuum. Thus, the couplings between the subshells can be treated in a close-coupling approach, whereas the coupling to the continuum in the perturbation theory. Full semiclassical calculations based on this idea, called the ''coupled-states approximation'' were reported by Amundsen and Jakubassa-Amundsen [55], using target hydrogenic Dirac wave functions and including multipole transitions up to $l=2$ for the electron final states. More refined coupled-channels calculations, accounting for the screening effect of the spectator electrons upon the couplings strength, have been performed by Legrand *et al.* [56]. A simplified coupled-channels calculation, known as the ''coupled-subshells model'' (CSM), has been proposed by Sarkadi and Mukoyama [48–51]. In the CSM model, one calculates the relative change of the ionization cross section caused by the subshell couplings effect assuming the dominance of transitions to the continuum with a minimum-energy transfers, and limiting the final states to those with $l_f=0,1$. Independently, the few-state coupled-channel model have been developed by Šmit and Orlić [57] on the basis of first-order approximation and in the united atom limit. All these models confirm the role of vacancy sharing process in L subshell ionization induced by heavy ions and reproduce the dominant tendencies of the L subshell ionization cross-section data [49–58]. However, in most of the works discussed, the role of coupling effects was confirmed for the relative L subshell ionization cross sections. The absolute data measured for heavy ions are still not satisfactorily reproduced by the theories discussed, particularly in the very adiabatic region [57,58] as well as for L_1 and L_3 subshells over a wide energy range [50,51,57–59].

The binding and polarization effects, which are not included in first-order calculations, are expected to contribute to the observed discrepancies for heavy ions due to a stronger perturbation of the initial electronic wave function. In the SCA calculations of Trautmann *et al.* [36,37], the binding effect was merely simulated in the extreme low- and high-velocity limits by bracketing it with, respectively, observed binding energies of the united projectile ion target atom (UA) and separated target atom (SA). The same approximation was used by Šmit and Orlić [57] in their few-state coupled-channel model. The binding correction derived in the ECPSSR theory using the hydrogenic wave functions is known to overestimate the binding effect [60]. The increase of the binding energies of the target electrons in the field of the projectile has been included in the simplified CSM model by Sarkadi and Mukoyama [48–51], in terms of the distortion approximation [61]. In order to quantify these effects systematically, more data concerning L subshell ionization by heavy ions are needed, particularly in the low-velocity regime.

It is well known that multiple-ionization of atoms might be a potential source of observed deviations. The vacancies, which are created in the shells that are above the L shell, alter the fluorescence and Coster-Kronig yields and radiative widths, the parameters that are used to convert the measured x-ray production cross sections to the L subshell ionization cross sections. Experimental studies on the influence of the multiple-ionization on L shell x-ray production are, however, rather scarce and generally performed with standard Si(Li) detectors [62,63]. Multiple-ionization probabilities have been usually estimated from the analysis of x-ray energy shifts [62,63]. In an alternative method [64], a change in the intensity ratios of L_3-M_1/L_3-$M_{4,5}$ and L_2-M_1/L_2-N_4 transitions in singly and multiply ionized atoms was used to infer multiple-ionization probabilities for $M_{4,5}$ and N_4 subshells.

However, the effects of multiple-ionization on x-ray spectra, intensity ratios of characteristic x-ray lines, and *L* x-ray production have never been studied systematically.

The aim of this work is a systematic study of *L* shell ionization of heavy atoms ($_{79}$Au, $_{83}$Bi, $_{90}$Th, and $_{92}$U) by $^{16}O^{q+}$ ions to investigate the role of multiple-ionization and coupling effects. The paper is organized as follows. The experimental setup and measurements are described in Sec. II. The data analysis is discussed in Sec. III, where detailed description of the applied method of analysis of x-ray spectra modified by the multiple-ionization effects is given. The effects of the multiple-ionization on the *L* shell fluorescence and Coster-Kronig yields and radiative emission rates, which are used to relate the ionization and x-ray production cross sections, are discussed in Sec. IV. In this section, in particular, an important effect of closing of strong Coster-Kronig transitions is described. In Sec. V, the *L* shell coupling effects are discussed within the CSM model to modify the SCA and ECPSSR ionization cross sections. The final discussion of the present results is given in Sec. VI and the work is concluded in Sec. VII.

II. EXPERIMENTAL PROCEDURE

The beams of oxygen $^{16}O^{q}$ ions of different charge states ($q=2-6+$) were obtained from the EN tandem accelerator at the Institute of Physics of the University of Erlangen-Nürnberg and from the heavy-ion cyclotron U-200P at the Heavy Ion Laboratory (HIL) of the Warsaw University. The energies of oxygen ions ranged from 6.4 to 70 MeV, which corresponds to 0.4-4.4 MeV/amu. The measurements for two highest energies of 51 and 70 MeV performed at HIL aimed to investigate a contribution of the electron-capture process to the *L* shell vacancy production, which is expected to be dominated by the direct ionization process for the asymmetric collisions studied. However, due to formation of *K* shell vacancies in the projectile by its charge-state equilibration in the target, the electron capture could play a role for high energies even for the projectiles with initially filled *K* shell ($q\leqslant 6$). Consequently, substantially enhanced *L* x-ray yields for highest projectile energies, with respect to the direct ionization, would indicate an importance of the electron capture (EC). This effect, however, has not been observed in the present data, thus indicating a minor role of the EC process for the studied systems.

The experimental details, which are important for the quality of the present data, are briefly described below. Thin targets (10–26 μg/cm^2) of Au, Bi, Th, and U, prepared by vacuum evaporation onto 10–15 μg/cm^2 carbon backings, were irradiated with typical beam currents of 2–30 nA. The ion-beam currents were monitored by charge collection on the target and in a Faraday cup. The targets were mounted at an angle of 30° with respect to the beam direction. The scattered ions were monitored by a Si surface-barrier detector placed at 150° relative to the beam axis. The x-rays were counted by a Canberra HPGe detector mounted outside the target chamber, perpendicul to the ion-beam axis. The x-rays, before reaching the active volume of the detector, passed through a 25-μm metallized Mylar chamber window, a 10-mm air gap, and a 25-μm beryllium detector window. An additional Mylar absorber (400-μm) was applied occasionally, to cut out intense and soft *M*-shell x-rays produced in the target. The resolution of the x-ray detector was measured to be 150 eV at 6.4 keV. Low x-ray detector count rates were maintained in order to minimize pileup and dead-time corrections. These corrections did not exceed 6%. In order to determine precisely the energies of individual x-ray transitions, after each change of the ion-beam energy, the radioactive x-ray sources were used to calibrate the energy of the x-ray detector. Additionally, to check the x-ray energy calibration, the *L* x-ray spectra induced by protons were measured. For these, the multiple-ionization effects are not expected to play a role and the energies of x-ray transitions observed correspond to their diagram values. In fact, the *L* x-rays induced by 3-MeV protons were found to agree indeed within experimental uncertainties, ± 5 eV, with their diagram values. As an example, typical *L* x-ray spectra of gold, induced by oxygen ions and protons are shown in Fig. 1, which clearly demonstrates a magnitude of the multiple-ionization effects observed for heavy ions.

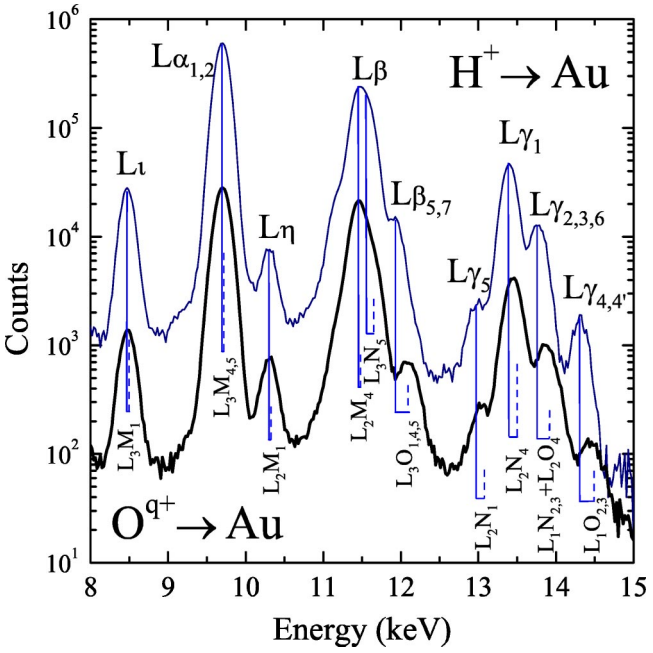

FIG. 1. Comparison of *L* x-ray spectra of Au excited by 3 MeV protons and 35.2 MeV oxygen ions, which shows the effects of x-ray line shifting and broadening due to the multiple ionization. The x-ray energies for proton impact coincide with the energies of diagram transitions (vertical solid lines) for single-vacancy configurations.

The efficiency of a HPGe x-ray detector was carefully measured by means of two different methods. Calibrated ($\pm 1.8\%$) radioactive sources of ^{57}Co, ^{133}Ba, ^{152}Eu, and ^{241}Am were used to determine the efficiency for x-ray energies above 6 keV. The x-ray detector efficiency, in the range between 2 keV and 28 keV, was obtained by bombarding thin targets of low-*Z* elements (from S to Sn) with 3-MeV protons. The resulting *K* x-ray yields were normalized to the number of elastically scattered ions. The ''reference'' *K* shell

ionization cross sections [66] and the screened Rutherford cross sections [67] were then used to determine the efficiency of the x-ray detector. Special attention was devoted to an accurate determination of the detector efficiency close to the Ge-K absorption edge, where L x-rays of the studied elements were expected to occur. A procedure originally suggested for Si(Li) detectors by Lennard and Philips [68] and subsequently developed by Pajek *et al.* [69] has been extended to HPGe detectors and used to analyze the detector efficiency in our case. We found that the observed increase of the detector efficiency above the Ge-K absorption edge could not be explained by the detector model used [69]. Therefore, the fitting was performed independently in two energy regions, below and above the Ge-K absorption edge, resulting in overall efficiency uncertainties of about 4%.

III. DATA ANALYSIS AND RESULTS

Figure 1 shows a typical spectrum of L x-rays produced by oxygen ions in Au target, in comparison with a proton induced spectrum. In both the spectra, the peaks corresponding to L_ℓ, $L\alpha_{1,2}$, $L\eta$, $L\beta$, $L\gamma_5$, $L\gamma_1$, $L\gamma_{2,3,6}$, and $L\gamma_{4,4'}$ transitions can be easily distinguished. In contrast to the proton induced spectrum, some x-ray peaks in the spectrum excited by oxygen ions are broadened and shifted towards higher energies. The widths and the energy shifts are characteristic for individual lines. Both features are evidences of existence of additional (spectator) vacancies in outer M, N, and O shells. Such multiple ionization results in the appearance of the so-called ''satellite lines,'' whose energies are higher than the energy of ''diagram'' transitions in a singly ionized atom. This effect is particularly pronounced for the outer M, N, and O shells of heavy target atoms bombarded by energetic heavy ions with energies of about 1 MeV/amu. This arises from the fact that in this condition the projectile velocity matches the electron velocity and thus the ionization probabilities for outer shells reach their highest values.

The multiple ionization is usually studied by means of high-resolution x-ray spectroscopy with crystal spectrometers [70–72] that resolve x-ray satellite structure originating from the multiple ionization, and provide information on ionization probabilities for different shells. In the following, we demonstrate that ionization probabilities for the outer M and N shells can still be obtained from a careful analysis of L x-ray line energy shifts and widths measured with 150–200 eV resolution of commonly used semiconductor x-ray detectors. Detailed description of this procedure can be found elsewhere [73], therefore here just a short synopsis of the method is presented.

Assuming the binomial character of the intensity distribution of x-ray satellites and their Gaussian energy spreads in the semiconductor detectors, the average energy shift ΔE of an x-ray line can be expressed in terms of the multiple-ionization probabilities per electron p_i and the energy shift per electron δE_i as follows:

$$\Delta E = \sum_i n_i p_i \delta E_i , \qquad (1)$$

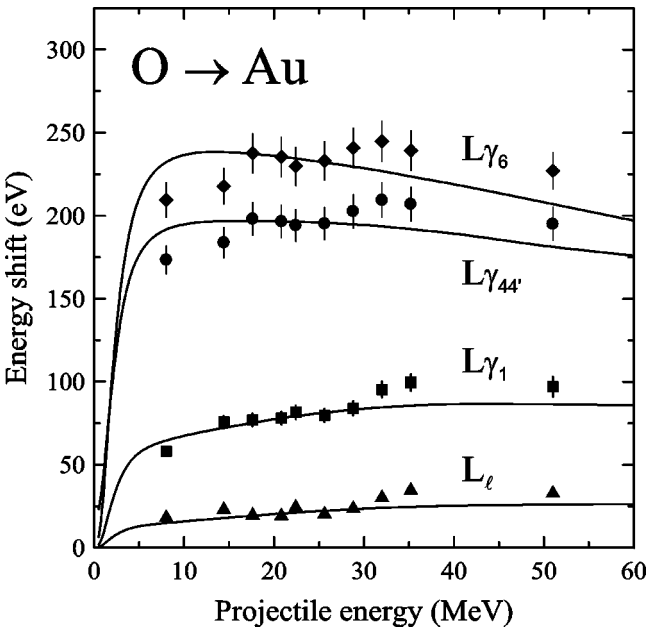

FIG. 2. Measured x-ray energy shifts of selected $L\gamma$ and L_l transitions in gold vs the energy of oxygen ions. Solid lines represent the expected projectile energy dependence of x-ray energy shifts, as calculated from Eq. (1), with the ionization probabilities taken from the ''geometrical model'' [65]. The theoretical predictions, which are not corrected for the vacancy rearrangement, are normalized to the data at impact energy 20.8 MeV.

where n_i is the number of electrons in $i=M$, N, and O shells. We note here that the present treatment neglects, in fact, a possible subshell dependence of p_i and δE_i, an assumption which is well justified for the M and N shells discussed [73]. Through such an approach we found additionally that the resulting broadened x-ray peaks can be described satisfactorily by Gaussian profiles with the widths given as [73]:

$$w = \left[w_G^2 + 8\ln 2 \sum_i n_i p_i (1-p_i) (\delta E_i)^2 \right]^{1/2}, \qquad (2)$$

where w_G denotes the width of a Gaussian peak unaffected by the multiple-ionization (e.g., as measured by proton bombardment) (Fig. 2). Figure 3 shows the energy profile of the $L\gamma_1$ transition in Au with a structure of satellite peaks due to spectator vacancies in the M and N shells. This figure exhibits the satellite structure convoluted with a Gaussian energy spread in the detector, for comparison with the shifted and broadened Gaussian peak whose mean value and width are fitted in our model [see Eqs. (1) and (2)]. We note here that an important ingredient of the present model is the introduction of ionization probability dependent peak widths in the analysis of x-ray spectra.

As we discuss in Ref. [73], this model allows for a reliable analysis of measured L x-ray spectra because the number of free parameters is substantially reduced to at most four fitting parameters determining the width and position of all peaks, namely, p_M, p_N, p_O, w_G and one additional intensity parameter for each transition in the group of $L\gamma$ x-ray lines.

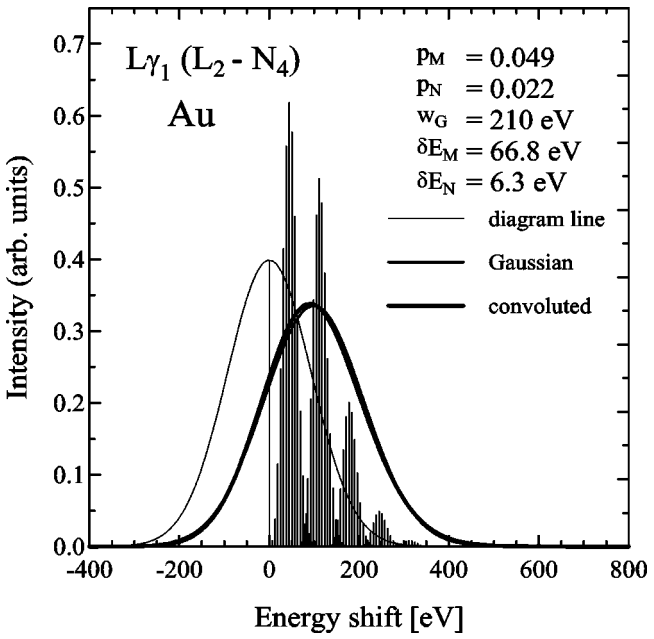

FIG. 3. Calculated satellite structure of the $L\gamma_1(L_2\text{-}N_4)$ x-ray transition in gold for multiply ionized M and N shells. The line profile, which is expected to be measured with a semiconductor detector (convoluted), is compared with the predicted Gaussian profile with mean shift and width given by Eqs. (1) and (2). The values of assumed ionization probabilities and x-ray energy shifts per vacancy for M and N shells as well as detector energy resolution, are shown in the figure. The profiles are plotted versus the x-ray energy shift with respect to the diagram transition.

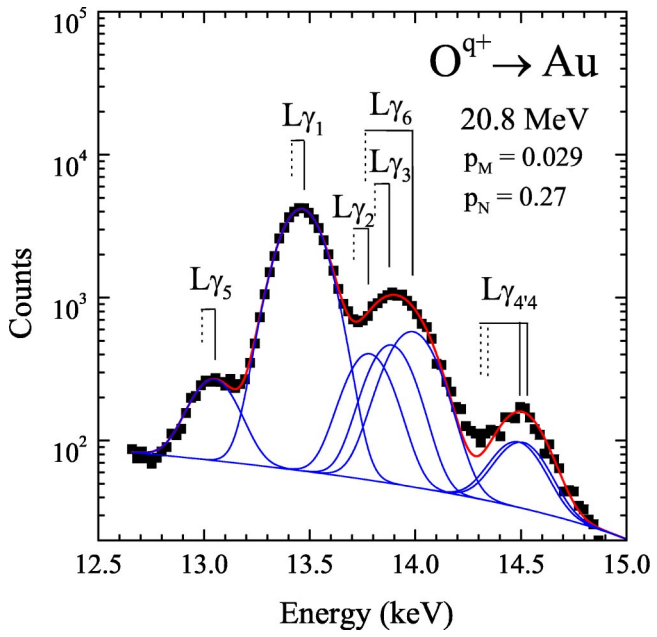

FIG. 4. The measured, and resolved, spectrum of $L\gamma$ x-ray transitions in gold excited by oxygen ions of energy 20.8 MeV. The ionization probabilities for M and N shells, derived by fitting the data, are shown in the figure.

The x-ray energy shifts and line broadening reflect a number of spectator vacancies, mainly, in the M, N, and O shells. The energy shifts of individual $L\gamma$ transitions per spectator vacancy in the pertinent subshells δE_i adopted in the present work were obtained using the relativistic Dirac-Fock calculations [74], assuming a single initial vacancy in the L_i-subshell and one spectator vacancy in the appropriate subshell of M, N or O-shell. The results of such Dirac-Fock calculations are given in Table I for the extreme elements studied, namely, Au and U, where the calculated shell-averaged energy shifts δE_i, appearing in Eqs. (1) and (2), are listed. A typical result of a fitting done for the $L\gamma$ spectrum of gold, using the method discussed, is shown in Fig. 4. In this spectrum, seven dominating transitions have been resolved: $L\gamma_5(L_2\text{-}N_1)$, $L\gamma_1(L_2\text{-}N_4)$, $L\gamma_2(L_1\text{-}N_2)$, $L\gamma_3(L_1\text{-}N_3)$, $L\gamma_6(L_2\text{-}O_4)$, $L\gamma_4(L_1\text{-}O_2)$, and $L\gamma_{4'}(L_1\text{-}O_3)$. It is inferred from the data that a number of spectator vacancies in M and N shells of the lighter target atoms (Au and Bi) is, on an average, about one and six, respectively. A degree of multiple-ionization, and correspondingly a number of vacancies, for heaviest target atoms (Th and U) is two times smaller. The number of additional vacancies in O shell remains rather uncertain because of their small contribution to the observed x-ray energy shifts. It is further obscured by a high (80%) uncertainty in determination of the x-ray shifts per vacancy in the O shell (see Table I). Moreover, the observed increased intensity of the $L\gamma_6$ line relative to the $L\gamma_1$ suggests that the outer O shell vacancies are quickly filled by a capture of loosely bound electrons from the valence band, before x-ray emission. This ''solid-state'' effect, which was observed earlier [75], becomes less important for increasing atomic number of the target atom. Fortunately, an inclusion of O shell in fitting the x-ray spectra by using Eqs. (1) and (2) has small influence on the resulting ionization probabilities for M and N shells. As we have checked, by fixing at extreme values $p_O=0$ or 1, this effect could modify the probabilities for M and N shells by less than 3%. Consequently, the multiple-ionization in O shell was neglected in analysis of x-ray spectra measured and consequently, the ionization probabilities for M and N shells were only derived from the data.

As a typical example, the measured ionization probabilities for M and N shells for gold bombarded by oxygen ion are shown in Fig. 5, in comparison with theoretical predictions. The measured probabilities for M and N shells, which

TABLE I. The calculated Dirac-Fock average energy shifts per spectator vacancy in M, N, and O shells for individual $L\gamma$ x-ray transitions in Au and U (in eV).

	Au			U		
Transition	δE_M	δE_N	δE_O	δE_M	δE_N	δE_O
$L\gamma_5(L_2\text{-}N_1)$	64.8	5.6		82.3	9.4	
$L\gamma_1(L_2\text{-}N_4)$	66.8	6.3		85.1	10.5	
$L\gamma_2(L_1\text{-}N_2)$	61.1	5.6		78.9	9.8	
$L\gamma_3(L_2\text{-}N_3)$	64.0	6.0		83.3	11.2	
$L\gamma_6(L_2\text{-}O_4)$	85.1	18.0	2.6	109.7	26.1	3.2
$L\gamma_{4'}(L_1\text{-}O_2)$	82.8	14.6	1.8	102.8	23.1	3.0
$L\gamma_4(L_1\text{-}O_3)$	86.9	15.4	2.1	105.7	25.7	4.2

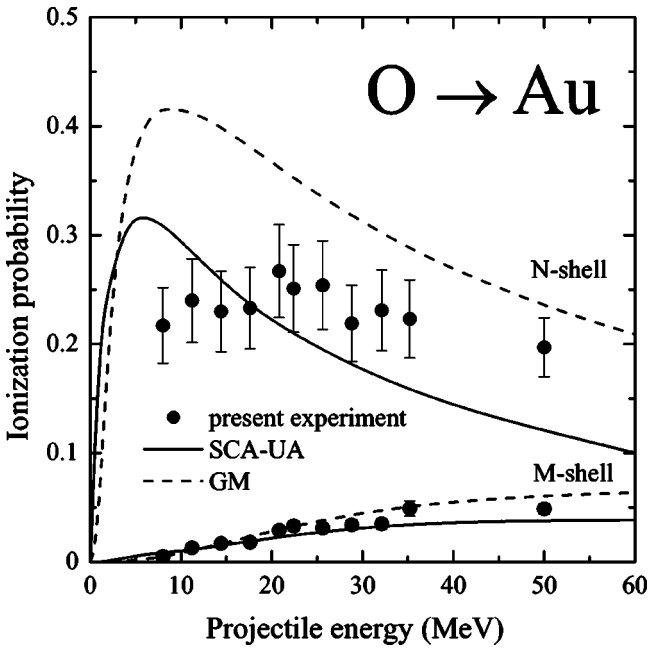

FIG. 5. Comparison of ionization probabilities for the *M*- and *N*-shell for gold bombarded by oxygen ions with the predictions of the semiclassical (SCA-UA) calculations and the ''geometrical model'' [65], both corrected for the vacancy rearrangement [76]. The probabilities were derived by fitting the x-ray spectra with the present method accounting for the multiple-ionization effects.

were extracted from *L* shell x-ray spectra, were compared with calculated probabilities for the zero impact parameter, modified for the vacancy rearrangement processes. Such probabilities were obtained from the semiclassical SCA-UA model [37,76] and the ''geometrical model'' (GM) [65,77,78]. An extended discussion of the multiple-ionization of *M* and *N* shells for studied systems can be found in our earlier work [76].

An important advantage of the proposed fitting method is that it allows one to separate reliably the $L\gamma_{2,3}(L_1\text{-}N_{2,3})$ and $L\gamma_6(L_2\text{-}O_4)$ x-ray transitions. That is because the energy shifts per vacancy, both in the *M* and *N* shells, are generally higher for transitions from the outer *O* shell. These lines, which cannot be resolved with a semiconductor detector if they arise from a single vacancy configurations, due to close transition energies, can be resolved in multiply ionized atoms (see Fig. 4). As is shown below, it has important consequences on the evaluation of the *L* subshell ionization cross sections.

The *L* x-ray production cross sections for L_ℓ, $L\alpha_{1,2}$, $L\eta$, $L\beta$, $L\gamma_5$, $L\gamma_1$, $L\gamma_{2,3}$, $L\gamma_6$, and $L\gamma_{4,4'}$ transitions were obtained from the measured x-ray intensities, using the procedure described in detail elsewhere [80]. The measured x-ray yields were normalized to the number of elastically scattered ions, and corrected for x-ray absorption and the projectile energy losses in a target [80]. The magnitude of this correction was always less than 10%. The influence of anisotropic emission of L_3 x-ray lines on measured cross sections, caused by collisionally induced alignment, was estimated using the alignment parameter A_{20} calculated by Trautmann and Baur [81]. Using these data, we have estimated that the influence of anisotropic emission of the L_3-subshell x-rays is negligible for our targets, being smaller than 2%. The total uncertainties of the measured x-ray cross sections were found to be between 9% and 13% for $L\alpha_{1,2}$ and $L\gamma_1$ transitions and 10–25% for $L\gamma_{2,3}$ transition. They are caused mainly by the 5% uncertainty of the x-ray detector efficiency determination, the statistical uncertainty of the x-ray yields (2–5%), and the 5% uncertainty of the target thickness monitored using Rutherford backscattering.

Table II lists the $L\alpha_{1,2}$, $L\gamma_1$, and $L\gamma_{2,3}$ and the total $L_{X_{tot}}$ x-ray production cross section measured in this work. As an example, a dependence of total *L* x-ray production cross section for Au, as a function of oxygen ion energy, is shown in Fig. 6. One finds here that the measured *L* x-ray production cross sections are generally in good agreement with the experimental results reported by other authors. The total *L* x-ray cross sections are compared with the predictions of the SCA calculations for direct ionization, both for the SA and the UA limits, as well as the the ECPSSR theory describing direct ionization and electron-capture processes. Figure 6 shows that a contribution of the electron capture is generally small, below 15%, as estimated from the ECPSSR theory for highest energy, and practically negligible for most of the present data. This means, in the light of a magnitude of discrepancies observed between the data and theoretical predictions (see Figs. 6 and 7), that it is enough to compare the present results with the theories describing the direct ionization process. Among the theories discussed, both the SCA-UA and ECPSSR calculations reproduce the total *L* x-ray cross sections for higher energies equally well, however, the low-energy results are systematically better described by the SCA-UA approach. In fact, this is the result one expects for adiabatic collisions $v_1/v_2 \ll 1$.

The measured x-ray production cross sections for $L\alpha_{1,2}$,$L\gamma_1$, and $L\gamma_{2,3}$ transitions in gold (see Table II), selected to show typical features in the data, are shown in Fig. 7. These results are compared here with the predictions of the SCA-UA and ECPSSR theories as well as the SCA-CSM calculations, which are discussed in detail in Sec.V. In general, the x-ray production cross sections for $L\alpha_{1,2}$, $L\gamma_1$, and $L\gamma_{2,3}$ are related to the L_1-, L_2-, and L_3-subshell ionization cross sections via the following relationships:

$$\sigma_{L\gamma_{2,3}} = \omega_1 \frac{\Gamma_{\gamma_{2,3}}}{\Gamma_1} \sigma_{L_1}, \tag{3a}$$

$$\sigma_{L\gamma_1} = \omega_2 \frac{\Gamma_{\gamma_1}}{\Gamma_2} [\sigma_{L_2} + f_{12}\sigma_{L_1}], \tag{3b}$$

$$\sigma_{L\alpha_{1,2}} = \omega_3 \frac{\Gamma_{\alpha_{1,2}}}{\Gamma_3} [\sigma_{L_3} + f_{23}\sigma_{L_2} + (f_{13} + f_{12}f_{23})\sigma_{L_1}], \tag{3c}$$

where the fluorescence (ω_1, ω_2, and ω_3) and Coster-Kronig (f_{12}, f_{13}, and f_{23}) yields can be found in Ref. [79] and the theoretical x-ray emission rates Γ in Ref. [82]. In these works, the theoretical *L* shell atomic parameters have been calculated for single-vacancy configurations. It is known,

TABLE II. The measured x-ray production cross sections (in barns) for $L\alpha_{1,2}$, $L\gamma_1$, and $L\gamma_{2,3}$ and total $L_{X_{tot}}$ for Au, Bi, Th, and U bombarded by ^{16}O ions. The ranges of experimental uncertainties are shown in the table.

	Au				Bi			
Energy (MeV)	$L\alpha_{1,2}$	$L\gamma_1$	$L\gamma_{2,3}$	$L_{X_{tot}}$	$L\alpha_{1,2}$	$L\gamma_1$	$L\gamma_{2,3}$	$L_{X_{tot}}$
6.4	2.88+0	4.40−1	1.24−1	6.69+0	2.11+0	3.81−1	9.99−2	4.98+0
8.0	7.68+0	9.19−1	1.57−1	1.61+1	6.10+0	8.49−1	1.37−1	1.31+1
11.2	2.87+1	2.68+0	4.48−1	5.51+1	2.25+1	2.26+0	3.70−1	4.29+1
14.4	5.80+1	4.73+0	8.85−1	1.07+2	4.46+1	3.92+0	5.61−1	8.20+1
17.6	1.08+2	8.48+0	1.51+0	1.96+2	7.34+1	6.00+0	7.62−1	1.33+2
20.8	1.78+2	1.31+1	2.22+0	3.19+2	1.28+2	9.92+0	1.28+0	2.28+2
22.4	2.20+2	1.56+1	2.69+0	3.92+2	1.50+2	1.74+1	2.53+0	2.73+2
25.6	3.11+2	2.15+1	3.86+0	5.39+2	2.07+2	1.51+1	2.19+0	3.64+2
28.8	3.88+2	2.59+1	5.17+0	6.81+2	2.94+2	2.09+1	2.97+0	5.13+2
32.1	5.62+2	3.66+1	7.27+0	9.82+2	3.97+2	2.78+1	4.31+0	6.91+2
35.2	6.56+2	4.20+1	8.23+0	1.14+3	4.90+2	3.35+1	5.44+0	8.53+2
51.0	1.61+3	9.63+1	2.20+1	2.91+3	1.19+3	7.07+1	2.10+1	1.52+3
70.0					1.76+3	1.08+2	3.40+1	3.15+3
Uncertainty (%)	9–12	10–13	10–25	7–9	10–12	10–12	10–15	8–10
	Th				U			
Energy (MeV)	$L\alpha_{1,2}$	$L\gamma_1$	$L\gamma_{2,3}$	$L_{X_{tot}}$	$L\alpha_{1,2}$	$L\gamma_1$	$L\gamma_{2,3}$	$L_{X_{tot}}$
6.4	7.65−1	1.92−1	6.22−2	2.16+0	2.03−1	5.40−2	1.51−2	5.52−1
8.0	2.36+0	4.39−1	7.93−2	5.83+0	6.13−1	1.48−1	2.70−2	1.67+0
11.2	9.72+0	1.32+0	2.28−1	2.10+1	3.66+0	5.58−1	1.08−1	8.08+0
14.4	2.17+1	2.46+0	4.09−1	4.44+1	1.79+1	2.20+0	4.25−1	3.66+1
17.6	4.16+1	4.25+0	7.05−1	8.20+1	3.54+1	3.91+0	6.78−1	7.21+1
20.8	6.63+1	6.32+0	9.54−1	1.28+2	5.24+1	5.35+0	8.24−1	1.00+2
22.4	9.86+1	9.16+0	1.37+0	1.89+2	7.77+1	7.75+0	1.17+0	1.48+2
25.6	1.22+2	1.10+1	1.50+0	2.31+2	8.86+1	8.50+0	1.18+0	1.67+2
28.8	1.75+2	1.50+1	2.03+0	3.27+2	1.31+2	1.20+1	1.64+0	2.43+2
32.1	2.18+2	1.82+1	2.35+0	4.04+2	1.62+2	1.43+1	1.88+0	2.98+2
35.2	2.61+2	2.14+1	2.75+0	4.79+2	2.34+2	2.04+1	2.58+0	4.27+2
51.0					4.34+2	2.34+1	4.17+0	7.06+2
70.0					1.05+3	5.77+1	1.10+1	1.72+3
Uncertainty (%)	10–12	10–12	10–15	7–9	10–12	10–12	11–25	7–10

however, that the fluorescence and Coster-Kronig yields as well as x-ray emission rates can be modified when atoms undergo multiple-ionization. Consequently, the effect of influence of multiple-ionization on the atomic parameters occurring in Eq. (3) has to be discussed in detail in order to compare the x-ray cross section data with the theoretical predictions for the ionization process. This effect will be discussed in Sec. IV.

The effect of multiple-ionization on the L subshell ionization cross sections, as derived from L x-ray cross sections, is even more severe. According to Eq. (3), the L subshell ionization cross sections can be derived from the x-ray production cross sections measured for the x-ray transitions from M ($L\alpha_{1,2}$) and N ($L\gamma_1$,$L\gamma_{2,3}$) shells. By doing so, the resulting L subshell ionization cross sections can be biased by the systematic uncertainties of L shell atomic parameters, which are modified by the multiple-ionization effects. There is another important ramification for the determination of the L_1-subshell ionization cross section. In earlier L shell ionization studies, the L_1-subshell cross section has been routinely derived from a sum of $L\gamma_{2,3}(L_1$-$N_{2,3})$ and $L\gamma_6(L_2$-$O_4)$ x-ray lines which were difficult to distinguish experimentally. In some experiments, the intensity of the $L\gamma_{2,3}$ line was obtained from the line intensities of $L\gamma_{2,3,6}$ and $L\gamma_1$ transitions [64,63], using the intensity ratio of $L\gamma_6(L_2$-$O_4)$ and $L\gamma_1(L_2$-$N_4)$ lines, which was determined theoretically for single-hole configurations [79]. However, the ratio of these lines for heavy-ion impact can be strongly modified due to different probabilities of the multiple-ionization in N and O shells. These effects can be further modified by the secondary processes such as the vacancy redistribution due to the Coster-Kronig and Auger transitions as well as the solid-state effects mentioned earlier [76]. We point out here that the fitting method of x-ray spectra adopted in the present work allows one to resolve $L\gamma_{2,3}$ and $L\gamma_6$ x-ray lines and thus to

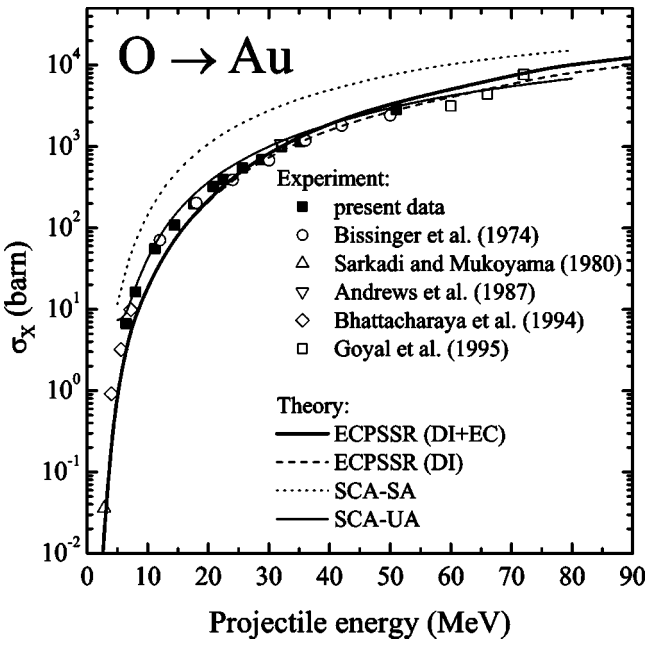

FIG. 6. Comparison of total L x-ray production cross sections for gold bombarded by oxygen ions with the predictions of the semiclassical calculations [37] for separated (SCA-SA) and united atom (SCA-UA) limits for direct ionization, as well as the ECPSSR theory [33,34] both for direct ionization (DI) and electron capture (EC), using single-vacancy L-shell decay rates [79]. The present data are compared with available results reported by other authors [14,15,41–43].

omit, in calculations, the uncertainty of the relative emission rate.

IV. MULTIPLE IONIZATION EFFECTS

In this section, the influence of the multiple-ionization effects on the L shell decay widths and, consequently, the fluorescence and Coster-Kronig yields as well as the radiative emission rates is discussed. Generally, the multiple-ionization can affect the radiative, Coster-Kronig, and Auger rates in three ways: (i) by reducing the number of electrons available for a given transition; (ii) by making the Coster-Kronig transition energetically forbidden, or closed, due to a change (typically increase) of the binding energies of electrons participating in the transition; and (iii) by modifying the wave functions of active electrons. In order to treat all these effects in multiply-ionized atoms, one needs complex atomic structure calculations for large number of multivacancy configurations. However, one expects that the wave function effects should not affect too much the relative quantities, such as the fluorescence, Coster-Kronig, and relative x-ray emission rates, due to a partial cancellation of the effects. This argumentation holds in particular for not too high ionization probabilities, such as in the present study, where they are below 25%. For this reason the multiple-ionization effect on the electronic wave functions is not discussed here. On the other hand, the other multiple-ionization effects mention above, namely the reduction of a number of electrons and closing of selected Coster-Kronig transitions, which can

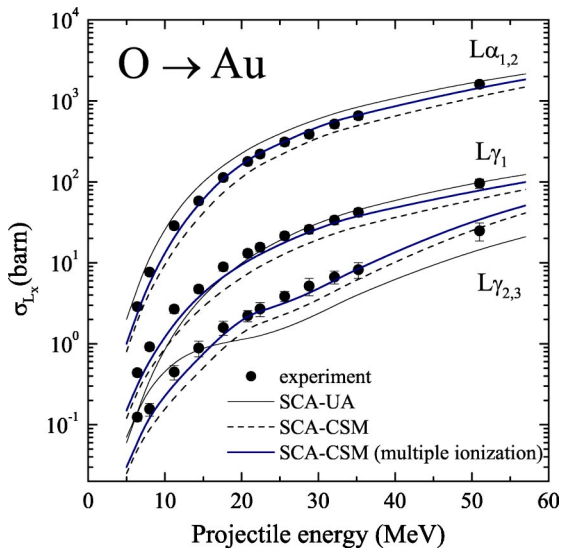

FIG. 7. Comparison of measured x-ray production cross sections for $L\alpha_{1,2}$, $L\gamma_1$, and $L\gamma_{2,3}$ transitions in gold bombarded by oxygen ions with the predictions, which are based on the semiclassical SCA-UA and SCA-CSM calculations of L subshell ionization cross sections and single-vacancy L-shell decay rates [see Eqs. (3)]. For comparison, the calculations for the SCA-CSM model were performed using L-shell rates modified by the multiple-ionization effects (see the text).

be accounted for in the multiple-ionized atoms in a simpler way, are discussed in the present paper in more details.

The simplest effect, which decreases the widths for both radiative as well as the radiationless transitions, is due to a reduction of the number of electrons available for a given transition. This can be accounted for by using the so-called statistical scaling [83] of the single-vacancy width by a fraction of available electrons, which, in turn, can be expressed in terms of the ionization probabilities for the shells of interest. We note, however, that for the discussed experiments, the L shell decay widths are mainly modified by the multiple-ionization in the M and N shells. Here, the estimated ionization probabilities for the L shell are negligibly small ($\lesssim 3\%$), as the influence of multiple-ionization in the O shell, is estimated to be below 5%, due to a small contribution of the transition involving O shell electrons to the L shell decay widths. Consequently, following the idea of statistical scaling of Larkins [83], the widths for radiative, Coster-Kronig, and Auger processes were scaled by appropriate statistical factors expressed in terms of the measured ionization probabilities for the M and N shells, assumed to be constant for a given shell. Generally, the statistical factors $(1-p_j)$, $(1-p_j)(1-p_k)$, or $(1-p_j)(1-p_j-1/N_j)/(1-N_j)$ were used if one or two active electrons, respectively, from different or the same shell were involved in the process. Here, N_j denotes the maximum number of electrons in a given shell. Using the measured ionization probabilities for M and N shells and the theoretical atomic widths [79,82], the L subshell decay widths for the individual radiative Γ_{ij}^{X}, Coster-Kronig Γ_{i-jk}^{CK}, and Auger Γ_{i-jk}^{A} processes were calculated. By summing up these widths, the partial L subshell decay widths for radiative $\Gamma_i^X(p_M, p_N)$, Coster-Kronig

TABLE III. The *L*-shell fluorescence (ω_i) and Coster-Kronig (f_{ij}) yields for Au, Bi, Th, and U for single-vacancy and multivacancy configurations. For single-vacancy configurations the semiempirical values of Krause [86] and the theoretical relativistic values of Chen *et al.* [79] are shown. For atoms multiple ionized by ^{16}O ions, the table shows the modified values of the relativistic yields of Chen *et al.* [79], which were obtained by applying the ''statistical scaling'' [83] (see the text), as well as their modified, configuration averaged [see Eq. (7)] values accounting for the effect of closing the Coster-Kronig (CK) transitions. These modifications were calculated using the measured ionization probabilities for the *M* and *N* shells. The values of statistically scaled yields are shown for the maximum projectile energy, while the ranges of the modified yields correspond to the projectile energy range.

Source	ω_1	ω_2	ω_3	f_{12}	f_{13}	f_{23}
	Gold ($_{79}$Au)					
Semiempirical[a]	0.107	0.334	0.320	0.140	0.530	0.122
Relativistic[b]	0.078	0.358	0.314	0.068	0.711	0.129
Statistical scaling	0.080	0.380	0.321	0.060	0.720	0.118
Closed CK transitions	0.174–0.191	0.372–0.378	0.312–0.321	0.086–0.086	0.420–0.388	0.110–0.118
	Bismuth ($_{83}$Bi)					
Semiempirical[a]	0.117	0.387	0.373	0.110	0.580	0.113
Relativistic[b]	0.099	0.416	0.358	0.055	0.700	0.119
Statistical scaling	0.101	0.433	0.362	0.048	0.707	0.106
Closed CK transitions	0.142–0.166	0.430–0.433	0.356–0.362	0.054–0.062	0.592–0.534	0.102–0.111
	Thorium ($_{90}$Th)					
Semiempirical[a]	0.161	0.479	0.463	0.090	0.570	0.108
Relativistic[b]	0.140	0.498	0.423	0.057	0.656	0.106
Statistical scaling	0.142	0.511	0.424	0.052	0.659	0.098
Closed CK transitions	0.142–0.145	0.506–0.511	0.418–0.425	0.043–0.041	0.664–0.666	0.098–0.101
	Uranium ($_{92}$U)					
Semiempirical[a]	0.176	0.467	0.489	0.080	0.570	0.167
Relativistic[b]	0.150	0.505	0.443	0.051	0.656	0.138
Statistical scaling	0.152	0.516	0.444	0.048	0.659	0.136
Closed CK transitions	0.153–0.156	0.528–0.533	0.438–0.445	0.041–0.041	0.658–0.657	0.105–0.104

[a]By Krause [86].
[b]By Chen *et al.* [79].

$\Gamma_{ij}^{CK}(p_M,p_N)$, and Auger $\Gamma_i^A(p_M,p_N)$ transitions were obtained to be further used to calculate the modified relative radiative widths as well as the fluorescence and Coster-Kronig yields. As we have found these effects modify the atomic *L*-shell parameters occurring in Eqs. (3) by less than 25% (see also Table III).

The multiple ionization, despite the statistical scaling effect discussed above, can also modify the *L* shell decay widths much stronger, namely, by making some transitions energetically forbidden. This happens, as we have shown earlier [84], for strong L_1-$L_3M_{4,5}$ Coster-Kronig transitions in gold multiply ionized by oxygen ions. In this case an increase of almost a factor of two in the fluorescence yield for L_1 subshell was reported [84] using a simplified model. However, in order to discuss this effect in more detail, in the present paper we report on the similar calculations performed for Au, Bi, Th, and U, resulting in the configuration-averaged *L* subshell fluorescence and Coster-Kronig yields.

The multiple-ionization, which modifies the binding energies of electrons, results in changing the energies of Coster-Kronig transitions which are called, in this case, the satellite Coster-Kronig transitions. For substantial ionization in the *M* and *N* shells, selected Coster-Kronig transitions, which are allowed in singly ionized atoms, can become energetically forbidden for multivacancy configurations. In order to discuss this effect, one has to consider the kinetic energy of the Coster-Kronig electron, which has to remain positive to the allowed transitions. The kinetic energy of the Coster-Kronig electron for the satellite transition with one additional vacancy, say $L_i(S^{-1})$-$L_jM_k(S^{-1})$ with $S=M,N$, can be expressed, using the ''Z+1 rule'' [85] to account for the screening effect, in terms of the electron binding energies $B_s(Z)$ as follows:

$$\varepsilon_{sat}^{i-jk}(s)=B_i(Z)-B_j(Z)-B_k(Z+1)+B_s(Z+1)-B_s(Z+2). \quad (4)$$

This expression can be easily generalized for the case of arbitrary number of vacancies *m* and *n* in the *M* and/or *N* shells [73], respectively, by introducing the average energy shift of energy of Coster-Kronig electron per vacancy, $\delta B_s = B_s(Z+1)-B_s(Z+2)$, namely,

$$\varepsilon_{sat}^{i-jk}(m,n)=\varepsilon_{diag}^{i-jk}+m\,\delta B_M+n\,\delta B_N, \quad (5)$$

where the electron energy for the diagram Coster-Kronig transition reads $\varepsilon_{diag}^{i-jk}=B_i(Z)-B_j(Z)-B_k(Z+1)$. The relativistic calculations of *L* shell Coster-Kronig energies are

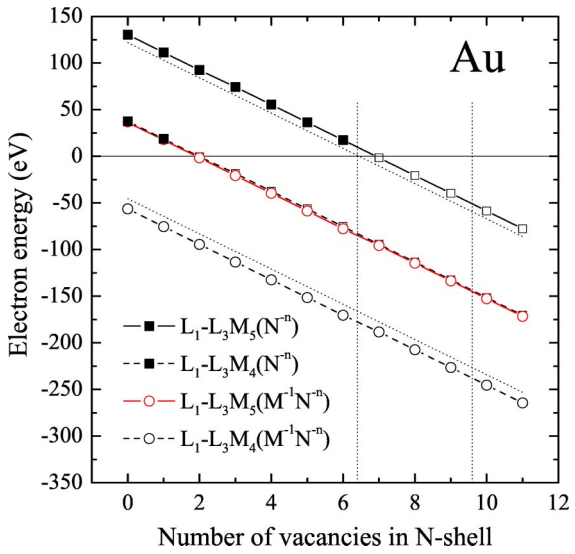

FIG. 8. Calculated Coster-Kronig energies [Eq. (5)] for the L_1-$L_3M_{4,5}$ transition in gold for different configurations with additional vacancies in M and N shells. The dotted lines mark the ranges of Coster-Kronig energies corresponding to the average numbers of vacancies expected for the range of projectile energies studied.

presently available [85] and those values were used in Eq. (5) to obtain the electron energies for the satellite Coster-Kronig transitions.

In this way, the electron energies for the satellite Coster-Kronig transitions $L_i(M^{-m}N^{-n})$-$L_jM_k(M^{-m}N^{-n})$ were calculated for each $M^{-m}N^{-n}$ spectator-vacancy configuration. We have found that for the studied heavy elements (Au, Bi, Th, and U), the following Coster-Kronig satellite transitions were energetically forbidden (closed) in multivacancy configurations: L_1-$L_3M_{4,5}$, L_1-$L_2N_{4,5}$, and a few weaker transitions. We note here that the strongest effect was observed for Au and Bi, for which the dominating L_1-$L_3M_{4,5}$ Coster-Kronig transitions, contributing about 50% to total decay width for L_1 subshell, were closed in multiply ionized atoms. This effect is demonstrated in Fig. 8, where the energies of Coster-Kronig electrons for the satellite transitions are shown for different multivacancy configurations. The effect of closing of selected Coster-Kronig transitions was accounted for in calculation of the partial Coster-Kronig decay widths for a given multivacancy configuration $M^{-m}N^{-n}$, by excluding from the sum those transitions which were found to be closed, namely,

$$\Gamma_{ij}^{CK}(m,n)=\sum_{k=open}\Gamma_{i-jk}^{CK}(p_M,p_N). \tag{6}$$

Consequently, two effects of the multiple-ionization on the L shell decay widths, namely, the statistical scaling of the decay rates and the closing of selected Coster-Kronig transitions, were accounted for, as discussed above. Finally, the Coster-Kronig widths modified in this way, as well as the modified radiative and Auger widths discussed earlier, were used to calculate the configuration averaged L subshell fluorescence yields:

$$\langle\omega_i\rangle=\sum_{m,n}P(m,n)\omega_i(m,n). \tag{7}$$

For the statistical weights $P(m,n)$ for each $M^{-m}N^{-n}$ configuration, the products of two binomial distribution factors were assumed, following the idea of the independent electron model [17] picture for the multiple-ionization process. With the measured ionization probabilities p_M and p_N for the M and N shell, respectively, and M and N denoting the maximum number of electrons in these shells, the statistical weight reads as follows:

$$P(m,n)=\binom{M}{m}p_M^m(1-p_M)^{M-m}\binom{N}{n}p_N^n(1-p_N)^{N-n}. \tag{8}$$

In the same way, the configuration averaged L shell Coster-Kronig yields $<f_{ij}>$ were calculated. We note here that due to the fact that the L shell relative radiative widths were not affected by the discussed effect of closing of Coster-Kronig transitions, their values were modified only by the statistical scaling effect, as discussed above. The numerical values of the modified L shell fluorescence and Coster-Kronig yields as well as the relative emission rates of interest for Au, Bi, Th, and U are summarized in Table III.

Generally, strong influence of the multiple-ionization effects on the L shell decay widths was found. While the effects of the statistical scaling modified the fluorescence and Coster-Kronig yields and relative emission rates less than 25%, the effect of closing strong Coster-Kronig transitions, mainly L_1-$L_3M_{4,5}$, in multiple-ionized Au and Bi atoms caused drastic, about a factor of two, increase of the fluorescence yields for L_1 subshell. For the heavier Th and U atoms this effect was not observed, mainly due to much higher energies for the diagram Coster-Kronig transitions for these elements. Figures 9 and 10 show the predicted changes of L shell fluorescence and Coster-Kronig yields for gold, for which the effect was the strongest, versus the projectile energy. Summarizing, we have evidenced substantial modifications of the L shell fluorescence and Coster-Kronig yields, and relative emission rates due to the multiple-ionization in the M and N shells. These effects, as we discuss in Sec.VI, are very important for deriving reliable L subshell ionization cross sections from the measured x-ray production cross sections [see Eqs. (3)].

V. THEORY OF IONIZATION CROSS SECTIONS

In the semiclassical approximation (SCA) [4,37], the projectile, assumed to move along the classical trajectory, induces the transition of electron from an initial state $i=L_1$, L_2, L_3 to free final state f in the continuum. In the SCA approach, this transition is treated quantum mechanically within the first-order time-dependent perturbation theory. In the impact-parameter formulation, the SCA ionization cross section σ_i^{SCA} is expressed as follows:

$$\sigma_i^{SCA}=2\pi\int_0^\infty bdb\sum_f|a_f(b,t=\infty)|^2, \tag{9}$$

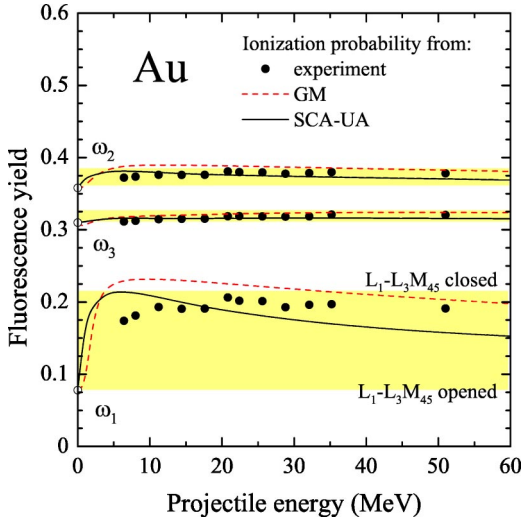

FIG. 9. Modified, average values [Eq. (7)] of *L*-shell fluorescence yields for gold atoms multiply ionized by oxygen ions. The calculations, including the effects of statistical scaling and closing of Coster-Kronig transitions, were performed using the experimental ionization probabilities for *M* and *N* shells, as well as their theoretical values obtained from the ''geometrical model'' (GM) [65,77] and the semiclassical SCA-UA calculations [37]. The shaded areas indicate the range of changes of the yields due to the effect of the closing of strong L_1-$L_3M_{4,5}$ Coster-Kronig transitions.

where b is the impact parameter and $a_f(b,t)$ is the transition amplitude at time t. In order to account for the L subshell coupling effects within the SCA approach, the ''coupled-subshells model'' (CSM) of Sarkadi and Mukoyama [51] was used here, which is a simplified version of the more general ''coupled-states model'' proposed by Amundsen and Jakubassa-Amundsen [55]. Assuming only the couplings between the initial L shell substates ($j=\{l,j,m_j\}$), the time evolution of the transition amplitude leading to the final state $f=\{\varepsilon_f,l_f\}$ is described by the following equations:

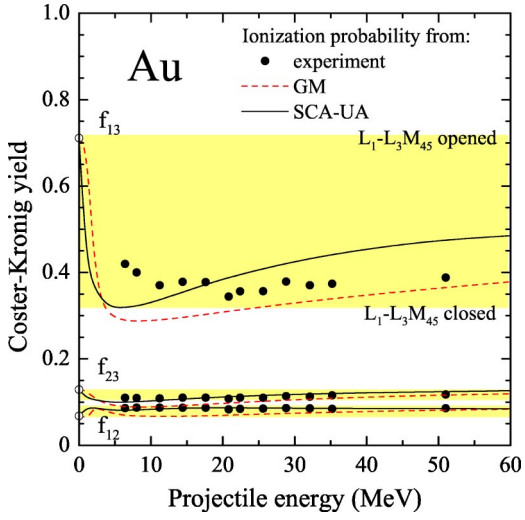

FIG. 10. Modified *L*-shell Coster-Kronig yields for gold atoms multiply ionized by oxygen ions. See the caption to Fig. 9 for a further description.

$$\frac{da_f}{dt}=-\frac{i}{\hbar}\sum_j V_{fj}(b,t)a_j(t) \tag{10}$$

and

$$\frac{da_j}{dt}=-\frac{i}{\hbar}\sum_{j'} V_{j'j}(b,t)a_{j'}(t). \tag{11}$$

Here the interaction matrix element reads

$$V_{jj'}(b,t)=\langle\Psi_j|\frac{-Z_1}{|\boldsymbol{r}-\boldsymbol{R}(t,b)|}|\Psi_{j'}\rangle\exp\left(\frac{i}{\hbar}(E_j-E_{j'})t\right), \tag{12}$$

with $\boldsymbol{R}(b,t)$ denoting the vector between projectile and the center of mass of the system and Ψ_j and E_j being the electronic wave function and energy in state j, respectively. In the first-order SCA treatment, one assumes that the L shell substates remain unperturbed in the collision and consequently, $a_j(t)=\delta_{ji}$, which leads to the following expression for the first-order ionization amplitude:

$$a_f^{(1)}(b,t=+\infty)=-\frac{i}{\hbar}\int_{-\infty}^{+\infty}dtV_{fi}(b,t). \tag{13}$$

The semiclassical SCA calculations of the L shell ionization cross sections were reported both for the straight-line and hyperbolic trajectories, describing the electronic states by using the hydrogenic nonrelativistic or relativistic as well as Dirac-Fock wave functions. The state-of-the-art SCA calculations were reported by Trautmann and co-workers [36,37], who also included the binding effect in the time-dependent manner [87], or in the simplified UA approximation. In this calculations, the recoil term was also included, but a magnitude of this process, in comparison to the direct Coulomb ionization, is negligible for the studied collision systems.

On the other hand, by solving the coupled-channels equations (10) and (11), the ionization amplitude $a_f^{(c)}(b,t=+\infty)$ accounting for the couplings between individual L shell substates can be obtained within the coupled-subshells model [51]. In this case, the ionization process is viewed as the transition from a ''mixed'' (or coupled) initial state to the continuum. In order to reduce the numerical complexity of solving the coupled-channels Eqs. (10) and (11), the following simplifying assumptions are adopted in the CSM model [51]: (i) the final states in the continuum have been restricted by regarding only the electronic states with zero kinetic energy $\varepsilon_f\approx 0$ and angular momentum of $l_f=0,1$; (ii) the multipole expansion of the perturbing potential is limited to the monopole, dipole, and quadrupole terms; and (iii) the matrix elements [Eq. (12)] were derived using screened nonrelativistic wave functions. Within such simplified SCA approach, the approximate coupled-channels cross sections were calculated using hyperbolic trajectories. This approach inherently includes the correction for the binding effect [51] in terms of the symmetric matrix elements $V_{jj}(b,t)$ in Eq. (10). Such approximate cross sections, due to a restricted number of the final states, have only relative character and thus can only be used to extract the correction factors to be applied to the

first-order cross sections, to account for the higher-order effects discussed. In fact, this can be achieved by dividing the approximate coupled-channels cross section $\sigma^{(c)_{app}}(\mathrm{hyp})$, which account for the coupling, binding, and hyperbolic trajectory effects, by the approximate first-order cross section $\sigma^{(1)_{app}}(\mathrm{sl})$ calculated within the same simplified approach using the straight-line trajectory. In this way, the approximate correction factors

$$c_i^{app}(\mathrm{coup,bin,hyp}) = \frac{\sigma_i^{(c)_{app}}(\mathrm{hyp})}{\sigma_i^{(1)_{app}}(\mathrm{sl})} \tag{14}$$

were obtained to correct the first-order SCA cross sections $\sigma_i^{SCA}(\mathrm{sl})$ calculated [37] for the straight-line (sl) trajectories. The coupled-channels calculations are generally known to underestimate the coupling effects (see, e.g., Refs. [51,55]), probably due to the simplifying approximations used to make the problem mathematically manageable. In fact, a similar feature was observed for the present CSM calculations. We have found that the calculated total L shell ionization cross sections, including the coupling effects, obtained by using the correction factors of Eq. (14) were smaller than the total cross sections, including only the correction for the binding and hyperbolic trajectory effects, in particular, for higher projectile energies for which the couplings are not expected to play any role. We have interpreted this effect as a systematic underestimation of the correction factors of Eq. (14) due to adopted approximations. In order to compensate for this effect, the correction factors of Eq. (14) were renormalized by taking into account that the couplings only redistribute the vacancies between L subshells [51], i.e., the total number of vacancies is conserved. Following this observation, normalization factor α, assumed to be constant for all L subshells, was introduced as follows:

$$\alpha = \frac{\Sigma_i \sigma_i^{SCA}(\mathrm{bin,hyp})}{\Sigma_i c_i^{app}(\mathrm{coup,bin,hyp})\sigma_i^{SCA}(\mathrm{sl})}. \tag{15}$$

The ionization cross sections, including the corrections for the binding and hyperbolic trajectory effects, $\sigma_i^{SCA}(\mathrm{bin,hyp})$, were obtained from the first-order $\sigma_i^{SCA}(\mathrm{sl})$ cross sections in a similar way, namely, as

$$\sigma_i^{SCA}(\mathrm{bin,hyp}) = \frac{\sigma_i^{(1)_{app}}(\mathrm{bin,hyp})}{\sigma_i^{(1)_{app}}(\mathrm{sl})}\sigma_i^{SCA-SA}(\mathrm{sl}). \tag{16}$$

The binding effect was accounted for in calculation of the approximate first-order cross section $\sigma_i^{(1)_{app}}(\mathrm{bin,hyp})$ by using the effective electron binding energy $E_i^{eff} = E_i + V_{ii}(b, t=0)$, as suggested in Ref. [33]. By applying this procedure, the values of $\alpha = 1.0-1.5$ were found and thus, the final correction factors were obtained as $c_i(\mathrm{coup,bin,hyp}) = \alpha c_i^{app}(\mathrm{coup,bin,hyp})$ for the studied systems. Finally, the theoretical SCA-CSM ionization cross sections, including the corrections for the coupling, binding, and hyperbolic trajectory effects were obtained:

$$\sigma_i^{SCA-CSM} = c_i(\mathrm{coup,bin,hyp})\sigma_i^{SCA-SA}(\mathrm{sl}). \tag{17}$$

It is worth noting that the SCA-CSM ionization cross sections of Eq. (17), despite including the correction for the L subshell couplings, also account for the binding effect [51], which is a real progress in comparison to the united-atom limit usually used to simulate the binding effect for rather slow $v_1/v_2 \lesssim 1$ collisions.

The direct ionization of inner-shell electrons by heavy projectiles can be also described within the plane-wave Born approximation (PWBA) [3]. This approach has been further developed to include the effects going beyond the first-Born PWBA. The ECPSSR theory of Brandt and Lapicki [33,34] accounts for the binding-polarization and Coulomb deflection (hyperbolic trajectory) effects as well as the corrections for the projectile energy loss and electronic relativistic wave functions. The ECPSSR theory, on the other hand, does not treat the L subshell coupling effects, which become important for heavy-ion impact ($Z_1 \gg 1$).

Following a discussion of the coupling effect within the SCA-CSM approach presented above, the correction factor purely describing the coupling effect can be obtained, to be further used to modify the ECPSSR cross sections for the direct ionization. In fact, the approximate correction factor $c_i^{app}(\mathrm{coup})$ can be derived from the simplified coupled-channels CSM model and the first-order SCA calculation as follows:

$$c_i^{app}(\mathrm{coup}) = \frac{\sigma_i^{(c)_{app}}(\mathrm{hyp})}{\sigma_i^{(1)_{app}}(\mathrm{bin,hyp})}. \tag{18}$$

Using the same arguments as discussed above, these correction factors $c_i^{app}(\mathrm{coup})$ have to be renormalized to compensate for the simplifications of the CSM calculations using factor α of Eq. (15) introduced earlier. Finally, the correction factors $c_i(\mathrm{coup}) = \alpha c_i^{app}(\mathrm{coup})$ obtained in this way from the CSM model were used to modify the ECPSSR ionization cross sections for the coupling effect as follows:

$$\sigma_i^{ECPSSR-CSM} = c_i(\mathrm{coup})\sigma_i^{ECPSSR}. \tag{19}$$

In this way, the L subshell coupling effects estimated from the CSM model were included in the ECPSSR theory for the direct ionization. The vacancy production by the electron capture to the projectile can also be included within the ECPSSR theory as the additive term. Such calculations are based on the Oppenheimer-Brinkman-Kramers approximation modified by Nikolaev [88] (OBKN) with the same corrections for the higher-order effects as for the direct ionization. However, the contribution of the electron capture is small compared with the direct ionization for the studied systems and energies. Consequently, the electron capture does not play a significant role in interpretation of the present data (see the following Sec. VI for detailed discussion). In this way, by using the presented approach, we were able to account for the coupling effects in both the SCA and the ECPSSR calculations.

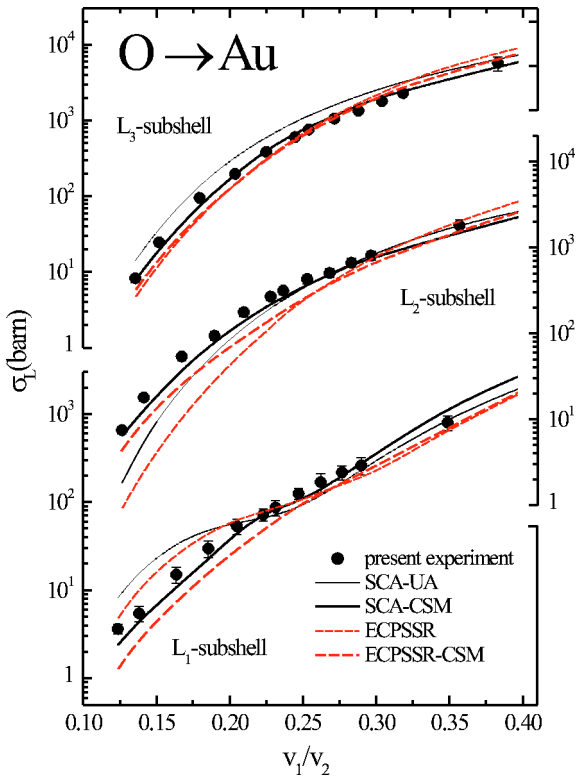

FIG. 11. Measured ionization cross sections for L_1, L_2, and L_3 subshells of gold bombarded by oxygen ions plotted vs relative projectile-electron velocity v_1/v_2. The data are compared with the predictions of the standard semiclassical SCA-UA calculations [37] and the ECPSSR theory [33,34] as well as their modifications accounting for the coupling effects, namely, the SCA-CSM and ECPSSR-CSM calculations (see the text).

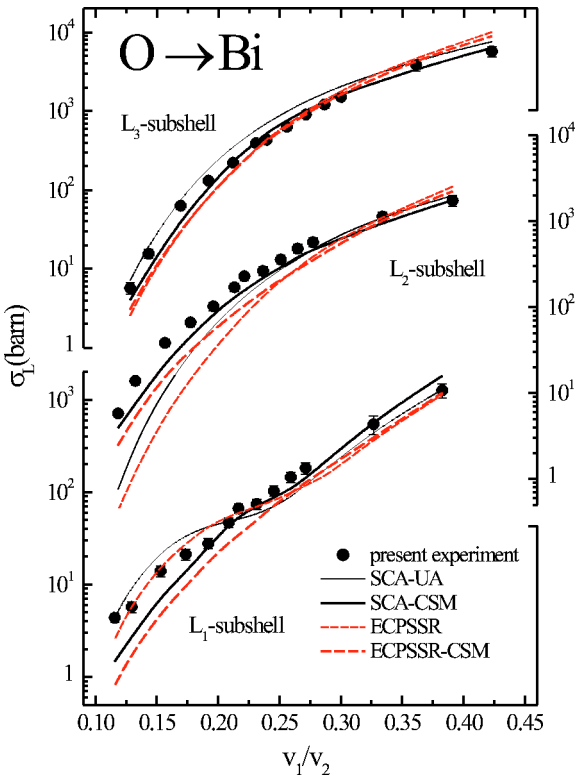

FIG. 12. The same as in Fig. 11, but for bismuth bombarded by oxygen ions.

VI. DISCUSSION

The measured ionization cross sections for L_1, L_2, and L_3 subshells of Au, Bi, Th, and U bombarded by oxygen ions, derived from Eqs. (3) using the modified L shell decay fluorescence and Coster-Kronig yields and emission rates (see Sec. IV), are shown in Figs. 11–14. These data are compared with the predictions of the semiclassical SCA calculations [37] for the direct ionization performed in the united-atom limit (SCA-UA) as well as the SCA-CSM model discussed in Sec. V, which accounts for the L subshell coupling effects. In Figs. 11–14, the predictions of the ECPSSR theory [33,34] and the modified ECPSSR-CSM calculations, which include corrections for the L subshell couplings adopted from the CSM model (see Sec. V), are also shown.

The ECPSSR calculations discussed account for the electron-capture process. For heavy ions, the electron capture may be important and it depends on the ionic charge-state q, which generally has some distribution for ions penetrating the solids. For the conditions of the present experiment, it was assumed that the equilibrium charge state fractions $F(q)$ were reached in the targets, having thicknesses in the range 10–26 μg/cm^2. Thus, the measured ionization cross sections have to be compared with the theoretical equilibrium cross sections σ_{eq} calculated for the equilibrium charge-state dis-

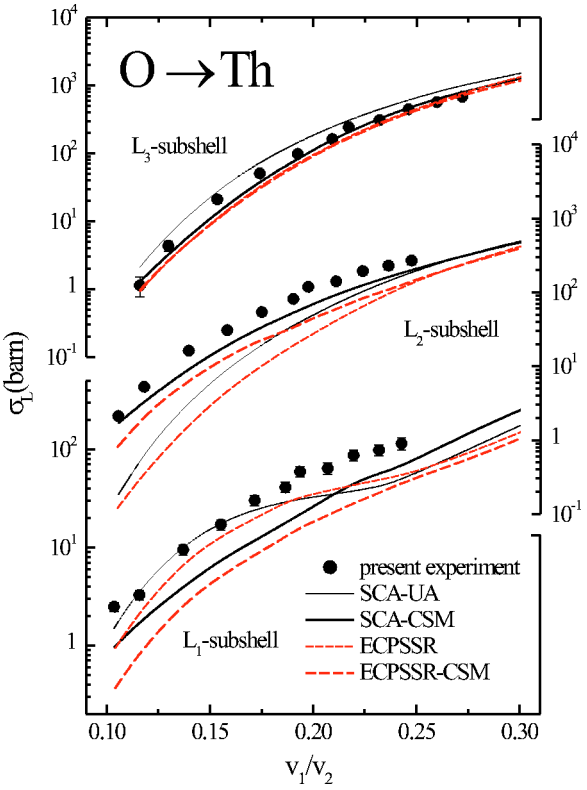

FIG. 13. The same as in Fig. 11, but for thorium bombarded by oxygen ions.

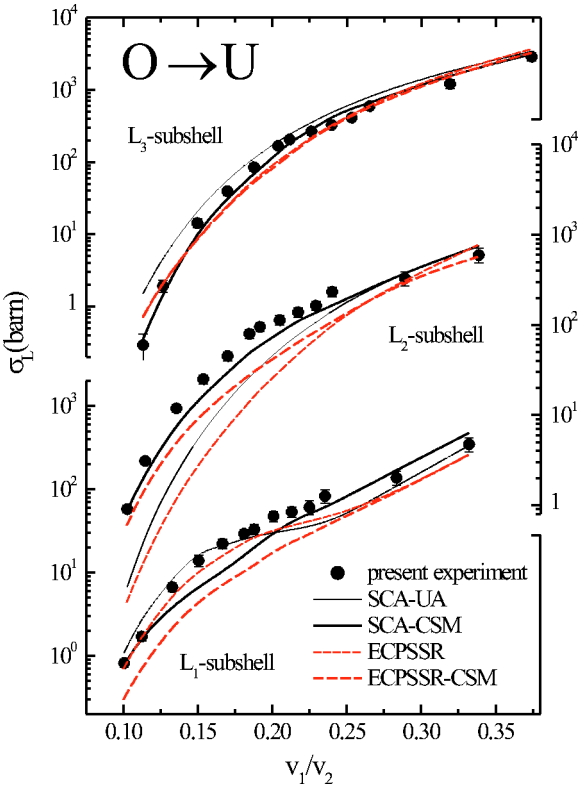

FIG. 14. The same as in Fig. 11, but for uranium bombarded by oxygen ions.

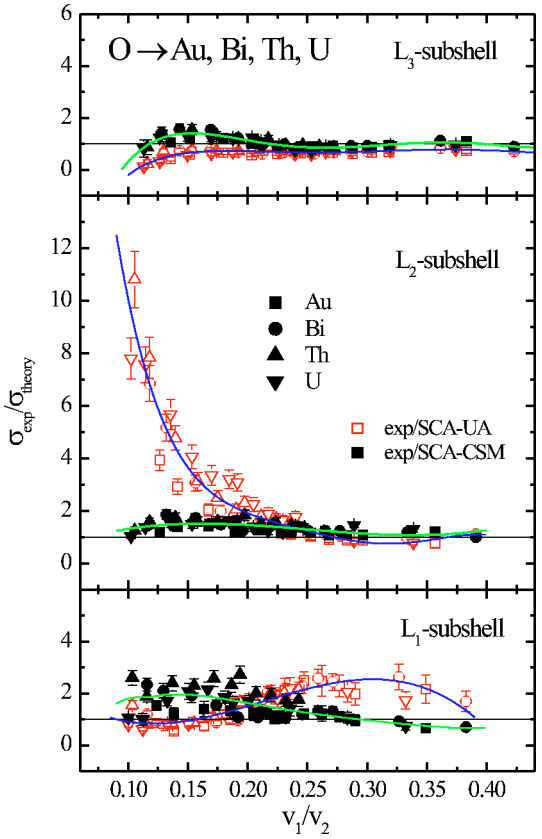

FIG. 15. The ratios of experimental-to-theoretical ionization cross sections for L_1, L_2, and L_3 subshells of Au, Bi, Th, and U atoms bombarded by oxygen ions plotted vs relative projectile-electron velocity v_1/v_2. The theoretical SCA-UA and SCA-CSM calculations are compared in order to show an improvement achieved by including L subshell coupling effects in the present theoretical approach.

tribution [89]. Noting that only the electron-capture cross sections $\sigma^{EC}(q)$ depend on the ion charge state, the following expression for the equilibrium total vacancy production cross section, i.e., a sum for direct ionization (DI) and electron capture (EC) processes, can be obtained:

$$\sigma_{eq} = \sigma^{DI} + \sum_q F(q)\sigma^{EC}(q). \tag{20}$$

The equilibrium ion charge fractions $F(q)$ were taken from Ref. [89]. It is worth noting here that this approach is an alternative approach to the well-known method [62] of measuring the ionization cross section for a given charge state, which requires extremely thin targets.

For asymmetric ($Z_1 \ll Z_2$) and rather slow ($v_1/v_2 \lesssim 1$) collisions studied, the contribution of electron capture [Eq. (20)] is generally small. In order to obtain more quantitative estimation of a contribution of the electron-capture process, dedicated measurements at higher projectile energies 51 MeV and 70 MeV were performed, for which a substantial fraction of completely stripped and one-electron projectiles is expected. In this case, an increased contribution of the EC process is anticipated, however, the data do not give any evidence of increased EC contribution. This observation is supported by the calculations of the EC cross sections, performed using the ECPSSR theory. These calculations, which are known to rather overestimate the EC cross sections, predict a contribution of this process to be smaller than 15% for highest projectile energies and practically negligible below 40 MeV. Consequently, the effect of the electron capture does not play, practically, a role in interpreting the data, in comparison with the direct ionization process, i.e., $\sigma_{eq} \approx \sigma^{DI}$. This observation justifies a comparison of the present data with the prediction of the SCA calculations, which describes only the direct ionization. In the light of these arguments the experimental L subshell ionization cross sections, which are shown in Figs. 11–14, could be compared with the predictions of the SCA calculations only for DI, and with the ECPSSR theory both for DI and EC processes [Eq. (20)], due to small contribution of the latter process.

A detailed comparison of the measured L subshell ionization cross sections for Au, Bi, Th, and U with theoretical predictions that neglect the coupling effects, namely, the SCA-UA and ECPSSR, as well as, on the other hand, account for the L subshell couplings within the CSM model, namely, the SCA-CSM and ECPSSR-CSM, can be found in Figs. 11–14. The conclusions, which can be drawn from this comparison are the following. An inclusion of L subshell couplings improves substantially the agreement of theoretical predictions (SCA-CSM and ECPSSR-CSM) with the data, as compared to the standard SCA-UA and ECPSSR calculations, which, e.g., underestimate the experimental cross sections for L_2 subshell at low energies almost by an

order of magnitude (see also Fig. 15). Similarly, the coupling effects improve drastically an agreement of the energy dependence of ionization cross sections for L_1 subshell. In particular, an absolute agreement observed for Au is very good, almost within experimental uncertainties, while for Bi, Th, and U, the calculations systematically underestimate the data. This effect can be possibly related to still insufficient modifications of L_1 subshell decay rates in multiply ionized atoms, which will be discussed later on. The results for L_3-subshell are reasonably well reproduced by the SCA-CSM calculations, but it is interesting to note that the coupling effects systematically improve an absolute agreement for this subshell.

Generally, the SCA-CSM calculations are systematically closer to the experimental data for all subshells and elements studied. For this reason, in Fig. 15, the measured L subshell ionization cross sections are compared systematically with the predictions of the SCA-CSM theory by plotting the expt/theory ratios versus relative projectile velocity v_1/v_2. This figure clearly shows the systematic trends in the data as well as an improvement achieved by including the L subshell couplings in theoretical treatment. This can be observed by comparing the ratios obtained for SCA-CSM with those for SCA-UA. Looking at systematic trends, it is worth noting that the SCA-CSM calculations agree with the high-energy data within 20–30%, while the residual discrepancies at medium and low energies are within 60% for L_2 and L_3 subshells, which we attribute to the approximations adopted for treating the coupling effects. Much bigger discrepancies, up to a factor of three for Bi, Th, and U, found at low energies for L_1 subshell can, in our opinion, manifest a necessity of even stronger modifications of the fluorescence yield for L_1 subshell as discussed in Sec. IV. We note that the effect of closing the L_1-$L_3M_{4,5}$ Coster-Kronig transitions for Au, which substantially increases the L_1-subshell fluorescence yields, results in much better agreement between the data and the SCA-CSM calculations.

In fact, adopted modifications of L shell decay widths include the statistical scaling and much stronger effect of closing, mainly, the L_1-$L_3M_{4,5}$ Coster-Kronig transitions in multiply ionized atoms. We note, that in the adopted approximate treatment of the latter effect, the modifications of electronic wave functions in multiply ionized atoms were neglected to simplify the problem. It is well known [90–92], however, that the wave function effect can possibly further enhance the closing of Coster-Kronig transitions, ultimately leading to a closure of L_1-$L_3M_{4,5}$ Coster-Kronig transitions for Bi, Th, and U, as predicted for Au, and partly for Bi, using the present approach (see Sec. IV). As we have calculated, this effect would result in an increase of L_1-subshell fluorescence yield by a factor of 2–3, which corresponds well, in magnitude, to the discrepancies observed for Bi, Th, and U at low energies (see Fig. 16). In order to answer this question more quantitatively, the complex calculations of the rates for radiationless transitions for multivacancy configurations are needed. Such calculations are, unfortunately, out of the scope of the present work.

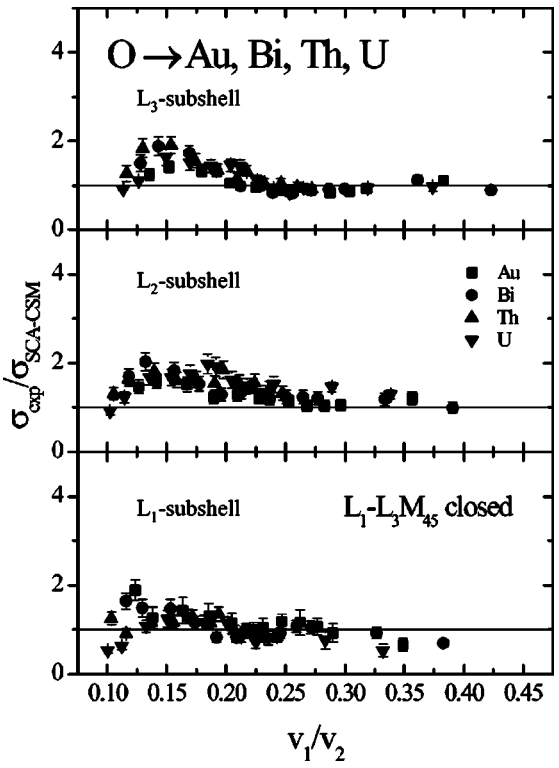

FIG. 16. The ratios of experimental ionization cross sections for L_1, L_2, and L_3 subshells of Au, Bi, Th, and U bombarded by oxygen ions, as obtained from Eqs. (3), using L-shell fluorescence and Coster-Kronig yields for assumed completely closed L_1-$L_3M_{4,5}$ Coster-Kronig transitions, and theoretical SCA-CSM cross sections plotted vs relative projectile-electron velocity v_1/v_2. Note that a substantial improvement is achieved, in particular for the L_1 subshell, as compared to Fig. 15.

VII. CONCLUSIONS

The L subshell ionization cross sections for Au, Bi, Th, and U have been studied systematically for incident oxygen ions for rather slow ($v_1/v_2 \lesssim 1$) collisions. The measured x-ray spectra were strongly affected by the multiple-ionization effects. The adopted method of analysis of x-ray spectra from multiply ionized atoms allowed the resolution of individual $L\gamma$ transitions and derivation of the ionization probabilities for multiply ionized M and N shell. A drastic change of L shell fluorescence and Coster-Kronig yields in multiply ionized atoms has been evidenced and discussed. In particular, by using a simple model we have showed that due to a closing of strong L_1-$L_3M_{4,5}$ Coster-Kronig transitions in multiply ionized Au, the decay rates for L_1 subshell can be modified by as much as a factor of two. Estimated modifications of L shell yields for heavier atoms (Bi, Th, and U) are smaller within adopted simplified model, but can be possibly further increased by the effect of modification of electronic wave functions in multiply ionized atoms.

The measured ionization cross sections for L_1, L_2, and L_3 subshells cannot be reproduced by standard theoretical approaches such as the SCA-UA and the ECPSSR theory. This is due to the neglect of coupling effects, which play an important role for heavier projectiles ($Z_1 \gg 1$), in particular

for lower energies. The couplings between L subshells were accounted for within the CSM, which was adopted to obtain the modified SCA-CSM and ECPSSR-CSM ionization cross sections. In particular, the present data are described reasonable well by the predictions of the SCA-CSM calculations.

Summarizing, we have shown that the multiple-ionization and coupling effects are very important for interpretation of the L shell ionization of atoms by heavy ions, which strongly perturb the L shell electrons. Present results partly explain a long-standing discrepancy observed between experiments and theoretical predictions of L shell ionization by heavy ($Z_1 \gg 1$) projectiles. In conclusion, it is worth emphasizing that the magnitude of the multiple-ionization effects, discussed for heavy projectiles, exceeds typical experimental uncertainties of the data and thus, a final interpretation of results depends strongly on the assumed model describing the relaxation of multiply ionized atom.

ACKNOWLEDGMENTS

This work was supported by the Federal Ministry for Research and Technology, Germany, under Contract No. POL-017-98 and by the Polish State Committee for Scientific Research (KBN) under Grant No. 5P03B-11420. We would like to express our thanks to the EN tandem accelerator staff at the University of Erlangen as well as to the crew of the Warsaw Heavy Ion Cyclotron for their kind collaboration during the experiments.

[1] P. Mokler and F. Folkmann, *Structure and Collisions of Ions and Atoms*, edited by Sellin (Springer, Berlin, 1978).
[2] J. Garcia, R. Fortner, and T. Kavanagh, Rev. Mod. Phys. **45**, 111 (1973).
[3] R. Merzbacher and H.W. Lewis, *Handbuch der Physik*, edited by S. Flügge (Springer, Berlin, 1958).
[4] J. Bang and J.M. Hansteen, K. Dan. Vidensk. Selsk. Mat. Fys. Medd. **31**, 13 (1959).
[5] W. Bambynek, B. Crasemann, R. Fink, H.-U. Freund, H. Mark, C. Swift, R. Price, and P.V. Rao, Rev. Mod. Phys. **44**, 716 (1972).
[6] *Atomic Inner Shell Processes*, edited by B. Crasemann (Academic Press, New York, 1978).
[7] C.H. Rutlege and R.L. Watson, At. Data Nucl. Data Tables **12**, 197 (1973).
[8] T.L. Hardt and R.L. Watson, At. Data Nucl. Data Tables **17**, 107 (1976).
[9] R.K. Gardner and T.J. Gray, At. Data Nucl. Data Tables **21**, 515 (1978).
[10] R.S. Sokhi and D. Crumpton, At. Data Nucl. Data Tables **30**, 49 (1984).
[11] H. Paul and J. Muhr, Phys. Rep. **135**, 47 (1986).
[12] G. Lapicki, J. Phys. Chem. Ref. Data **18**, 111 (1989).
[13] I. Orlić, C.H. Sow, and S.M. Tang, At. Data Nucl. Data Tables **56**, 59 (1994).
[14] G. Bissinger, P.H. Nettles, S.M. Shafroth, and A.W. Waltner, Phys. Rev. A **10**, 1932 (1974).
[15] M.C. Andrews, F.D. McDaniel, J.L. Duggan, P.D. Miller, P.L. Pepmiller, H.F. Krause, T.M. Rosseel, L.A. Rayburn, R. Mehta, and G. Lapicki, Phys. Rev. A **36**, 3699 (1987).
[16] R. Mehta, J.L. Duggan, F.D. McDaniel, M.C. Andrews, G. Lapicki, P.D. Miller, L.A. Rayburn, and A.R. Zander, Phys. Rev. A **28**, 2722 (1983).
[17] J.H. McGuire and L. Weaver, Phys. Rev. A **16**, 41 (1977).
[18] B.H. Choi, E. Merzbacher, and G.S. Khandelwal, At. Data Nucl. Data Tables **5**, 291 (1973).
[19] R. Rice, G. Basbas, and F.D. McDaniel, At. Data Nucl. Data Tables **20**, 503 (1977).
[20] D.E. Johnson, G. Basbas, and F.D. McDaniel, At. Data Nucl. Data Tables **24**, 1 (1979).
[21] J.M. Hansteen and O.P. Mosebekk, Nucl. Phys. A **201**, 541 (1973).
[22] J.M. Hansteen, O.M. Johnsen, and L. Kocbach, At. Data Nucl. Data Tables **15**, 305 (1975).
[23] L. Kocbach, J. Phys. B **9**, 2269 (1976).
[24] R.W. Brandt and I. Sellin, Phys. Rev. **151**, 56 (1966).
[25] A. Amundsen, J. Phys. B **10**, 2177 (1977).
[26] M. Pauli and D. Trautmann, J. Phys. B **11**, 667 (1978).
[27] D. Jamnik and Č. Zupancič, K. Dan. Vidensk. Selsk. Mat. Fys. Medd. **31**, 1 (1957).
[28] B.H. Choi, Phys. Rev. A **4**, 1002 (1971).
[29] P. Amundsen and L. Kocbach, J. Phys. B **8**, L122 (1975).
[30] M. Pauli, F. Rösel, and D. Trautmann, J. Phys. B **11**, 2511 (1978).
[31] G. Basbas, W. Brandt, and R. Laubert, Phys. Rev. A **7**, 983 (1973).
[32] W. Brandt and G. Lapicki, Phys. Rev. A **10**, 474 (1974).
[33] W. Brandt and G. Lapicki, Phys. Rev. A **20**, 465 (1979).
[34] W. Brandt and G. Lapicki, Phys. Rev. A **23**, 1717 (1981).
[35] D. Trautmann and F. Rösel, Nucl. Instrum. Methods **169**, 259 (1980).
[36] D. Trautmann, F. Rösel, and G. Baur, Nucl. Instrum. Methods Phys. Res. **214**, 21 (1983).
[37] D. Trautmann and T. Kauer, Nucl. Instrum. Methods Phys. Res. B **42**, 449 (1989).
[38] Z. Halabuka, W. Preger, and D. Trautmann, Z. Phys. D: At., Mol. Clusters **29**, 151 (1994).
[39] J. Semaniak *et al.*, Nucl. Instrum. Methods Phys. Res. B **86**, 185 (1994).
[40] J. Semaniak *et al.*, Phys. Rev. A **52**, 1125 (1995).
[41] L. Sarkadi and T. Mukoyama, J. Phys. B **13**, 2255 (1980).
[42] D. Bhattacharya, M. Sarkar, M.B. Chatterjee, P. Sen, G. Kuri, D.P. Mahapatra, and G. Lapicki, Phys. Rev. A **49**, 4616 (1994).
[43] D.P. Goyal, J.S. Braich, S. Murlithar, B.P. Singh, and H.R. Verma, Z. Phys. D: At., Mol. Clusters **35**, 155 (1995).
[44] L. Sarkadi and T. Mukoyama, J. Phys. B **14**, L255 (1981).
[45] K. Finck, W. Jitschin, and H.O. Lutz, J. Phys. B **16**, L409 (1983).
[46] L. Sarkadi and T. Mukoyama, Nucl. Instrum. Methods Phys. Res. B **4**, 296 (1984).
[47] L. Sarkadi, J. Phys. B **19**, 2519 (1986).

[48] L. Sarkadi, J. Phys. B **19**, L755 (1986).
[49] L. Sarkadi and T. Mukoyama, J. Phys. B **20**, L559 (1987).
[50] L. Sarkadi and T. Mukoyama, J. Phys. B **23**, 3849 (1990).
[51] L. Sarkadi, T. Mukoyama, and Ž. Šmit, J. Phys. B **29**, 2253 (1996).
[52] M.H. Martir, A.L. Ford, J.F. Reading, and R.L. Becker, J. Phys. B **15**, 2405 (1982).
[53] G. Mehler, T. De Reus, U. Müller, J. Reinhardt, B. Müller, W. Greiner, and G. Soff, Nucl. Instrum. Methods Phys. Res. A **240**, 559 (1987).
[54] G. Mehler, J. Reinhardt, B. Müller, W. Greiner, and G. Soff, Z. Phys. D: At., Mol. Clusters **5**, 143 (1987).
[55] P.A. Amundsen and D.H. Jakubassa-Amundsen, J. Phys. B **21**, L99 (1988).
[56] I.C. Legrand, V. Zoran, R. Dörner, H. Schmidt-Böcking, A. Berinde, D. Fluerasu, and C. Ciortea, J. Phys. B **25**, 189 (1992).
[57] Ž. Šmit and I. Orlić, Phys. Rev. A **50**, 1301 (1994).
[58] I. Bogdanović, S. Fazinić, M. Jakšić, and Ž. Šmit, Phys. Rev. A **56**, 2860 (1997).
[59] M. Sarkar, M.B.C.D. Bhattacharya, P. Sen, G. Kuri, D.P. Mahapatra, and G. Lapicki, Nucl. Instrum. Methods Phys. Res. B **103**, 23 (1995).
[60] M. Vigilante, P. Cuzzocrea, N. De Casare, F. Murolo, E. Perillo, and G. Spadaccini, Nucl. Instrum. Methods Phys. Res. B **51**, 232 (1990).
[61] L. Kocbach, Nucl. Instrum. Methods Phys. Res. B **4**, 248 (1984).
[62] G.H. Pepper, R.D. Lear, T.J. Gray, R.P. Chaturvedi, and C.F. Moore, Phys. Rev. A **12**, 1237 (1975).
[63] S. Ito, M. Shoji, N. Maeda, R. Katano, T. Mukoyama, R. Ono, and Y. Nakayama, J. Phys. B **20**, L597 (1987).
[64] C. Berinde, C. Ciortea, A. Enulescu, D. Fluerasu, G. Hock, I. Piticu, L. Sarkadi, B. Sulik, and V. Zoran, J. Phys. B **20**, L481 (1987).
[65] B. Sulik, G. Hock, and D. Berényi, J. Phys. B **17**, 3239 (1984).
[66] H. Paul and J. Sacher, At. Data Nucl. Data Tables **42**, 105 (1989).
[67] E. Huttel, W. Arnold, H. Baumgart, and G. Clausnitzer, Nucl. Instrum. Methods Phys. Res. B **12**, 193 (1985).
[68] W.N. Lennard and D. Philips, Nucl. Instrum. Methods **166**, 521 (1979).
[69] M. Pajek, A.P. Kobzev, R. Sandrik, R.A. Ilkhamov, and S.H. Khusmurodov, Nucl. Instrum. Methods Phys. Res. B **42**, 346 (1989).
[70] P. Rymuza, Z. Sujkowski, M. Carlen, J.-C. Dousse, M. Gasser, J. Kern, B. Penry, and C. Rhême, Z. Phys. D: At., Mol. Clusters **14**, 37 (1989).
[71] M.W. Carlen *et al.*, Phys. Rev. A **46**, 3893 (1992).
[72] C. Heitz, J. Larcher, G.J. Costa, A. Pape, Y. El Masri, T. Keutgen, I. Tilquin, F. Hanappe, and P. Duhamel, Z. Phys. D: At., Mol. Clusters **42**, 15 (1997).
[73] D. Banaś *et al.*, Nucl. Instrum. Methods Phys. Res. B **195**, 233 (2002).
[74] J. Desclaux, Comput. Phys. Commun. **9**, 31 (1975).
[75] D. Banaś, J. Braziewicz, U. Majewska, M. Pajek, J. Semaniak, T. Czyżewski, M. Jaskóła, W. Kretschmer, T. Mukoyama, and D. Trautmann, J. Phys. B **33**, L793 (2000).
[76] D. Banaś, J. Braziewicz, A. Kubala-Kukuś, U. Majewska, M. Pajek, J. Semaniak, T. Czyżewski, M. Jaskóła, W. Kretschmer, and T. Mukoyama, Nucl. Instrum. Methods Phys. Res. B **164/165**, 344 (2000).
[77] B. Sulik, I. Kádár, S. Ricz, D. Varga, J. Végh, G. Hock, and D. Berényi, Nucl. Instrum. Methods Phys. Res. B **28**, 509 (1987).
[78] G. Hock, B. Sulik, J. Végh, I. Kádár, S. Ricz, and D. Varga, Nucl. Instrum. Methods Phys. Res. A **240**, 475 (1985).
[79] M.H. Chen, B. Crasemann, and H. Mark, Phys. Rev. A **24**, 177 (1981).
[80] J. Braziewicz, J. Semaniak, T. Czyżewski, L. Głowacka, M. Jaskóła, M. Haller, R. Karschnik, W. Kretschmer, and T. Mukoyama, J. Phys. B **27**, 1535 (1994).
[81] D. Trautmann and G. Baur, Nucl. Instrum. Methods Phys. Res. A **40/41**, 345 (1989).
[82] J.H. Scofield, At. Data Nucl. Data Tables **14**, 121 (1974).
[83] F.P. Larkins, J. Phys. B **4**, L29 (1971).
[84] D. Banaś, J. Braziewicz, M. Pajek, J. Semaniak, T. Czyżewski, I. Fijał, M. Jaskóła, W. Kretschmer, T. Mukoyama, and D. Trautmann, J. Phys. B **35**, 3421 (2002).
[85] M.H. Chen, B. Crasemann, K.N. Huang, M. Aoyagi, and H. Mark, At. Data Nucl. Data Tables **19**, 97 (1977).
[86] M.O. Krause, J. Phys. Chem. Ref. Data **8**, 307 (1979).
[87] M. Pajek, A.P. Kobzev, D. Trautmann, and T. Kauer, Nucl. Instrum. Methods Phys. Res. B **52**, 109 (1990).
[88] V.S. Nikolaev, Zh. Eksp. Teor. Fiz. **51**, 1263 (1966) [Sov. Phys. JETP **24**, 847 (1967)].
[89] K. Shima, T. Mikumo, and H. Tawara, At. Data Nucl. Data Tables **34**, 3813 (1986).
[90] M.H. Chen and B. Crasemann, Phys. Rev. A **12**, 959 (1975).
[91] M.H. Chen, B. Crasemann, K.R. Karim, and H. Mark, Phys. Rev. A **24**, 1845 (1981).
[92] M.H. Chen, Phys. Rev. A **40**, 2758 (1989).